The Non-Resonant Magnetic X-ray Scattering Cross Section of MnF$_2$. 2. High-Energy X-ray Diffraction at 80 keV

J. Strempfer,[a] T. Brückel,[a]* U. Rütt,[a] J. R. Schneider,[a] K.-D. Liss[b] and T. Tschentscher[b]

[a]*Hamburger Synchrotronstrahlungslabor HASYLAB at Deutsches Elektronen-Synchrotron DESY, Notkestrasse 85, D-22607 Hamburg, Germany, and* [b]*European Synchrotron Radiation Facility ESRF, BP 220, F-38043 Grenoble CEDEX, France. E-mail: brueckel@desy.de*

This paper is dedicated to Professor W. Prandl on the occasion of his 60th birthday

Abstract

Results of high-energy non-resonant magnetic X-ray diffraction experiments performed on the model system MnF$_2$ at a photon energy of 80 keV are presented. A surprisingly high peak intensity of the magnetic 300 reflection of 13 000 photons s^{-1} in the three-crystal mode and 19 000 photons s^{-1} in the two-crystal mode, with a peak-to-background ratio of 230:1 and 10:1, respectively, has been achieved. At 80 keV, the penetration depth is 7 mm. When the path length of the beam through the crystal is varied, the effect of volume enhancement of the intensity diffracted by magnetic reflections is demonstrated. The Q dependence of the magnetic and the charge Bragg reflections has been measured and agrees well with theory. The measurement of the temperature dependence of the sublattice magnetization allows a very accurate determination of the critical exponent $\beta = 0.333\,(3)$ and the Néel temperature $T_N = 67.713\,(2)$ K. Finally, the multiple charge scattering is discussed, which is very pronounced for the magnetic reflections of MnF$_2$.

1. Introduction

We have reported a study of non-resonant magnetic X-ray diffraction from MnF$_2$ for photon energies between 5 and 12 keV in the preceding paper, hereafter referred to as paper 1 (Brückel *et al.*, 1996), where the model system MnF$_2$ and the X-ray scattering cross section are discussed in detail.

While most X-ray diffraction studies of magnetic materials nowadays make use of resonant exchange scattering, we pointed out in the *Introduction* to paper 1 that it is important to develop techniques for non-resonant X-ray scattering, mainly because resonance enhancements at the K edges of $3d$ and $4d$ transition metals are very small. In this paper, we present an alternative approach to obtain higher diffracted intensities, namely the volume enhancement due to an increase of the penetration depth by using very hard

X-rays with energies above 80 keV. Clearly, the penetration depth is larger for lighter elements (transition-metal compounds as compared to lanthanides and actinides). Therefore, this new technique complements resonant exchange scattering at its best. We also want to point out some further advantages of high-energy diffraction: simple windowless sample environment; sensitivity to true bulk properties; very high intrinsic Q-space resolution; extinction-free precision measurement of magnetic structure factors owing to the short wavelength and the small cross section; enhancement of weak signals relative to charge reflections owing to large scattering volumes; neutron and photon measurements of bulk properties from the same crystal.

The development of magnetic X-ray scattering and the possibility of using high-energy X-rays to study magnetic materials is closely correlated to the advancement of X-ray sources. For medium-energy X-ray diffraction with penetration depths of a few μm, only a near-surface region is accessible as discussed in paper 1, while neutrons are scattered from the bulk of the sample. In recent years, harder X-rays have become available with high photon fluxes. In this paper, measurements on MnF$_2$ using X-rays with a wavelength of $\lambda = 0.155$ Å corresponding to a photon energy of 80 keV are presented. The absorption length is about $1/\mu = 7$ mm. Therefore, we observe scattering by the bulk material as is the case in neutron scattering. This is especially important for the study of magnetically disordered materials. As was shown for the random field magnet Mn$_{0.75}$Zn$_{0.25}$F$_2$ (Hill, Feng, Birgeneau & Thurston, 1993), surface preparation affects drastically the magnetic properties in a near-surface region since domains are pinned to surface defects, like scratches. While this is a rather interesting phenomenon, the intrinsic disorder effects can safely be studied only with a true bulk probe. Moreover, if the X-ray energy is varied from 8 to 100 keV and thus the path length of the beam through the crystal, it will be possible to distinguish near-surface and bulk properties. The Q-space resolution obtained with a triple-crystal

diffractometer is about one order of magnitude higher than for high-resolution neutron diffraction (Neumann, Rütt, Bouchard, Schneider & Nagasawa, 1994). For a detailed discussion of the general aspects of high-energy synchrotron-radiation experiments as a probe to study condensed matter, we refer to Schneider (1995).

Information on the spin-density distribution in the lattice can be obtained from the X-ray intensities of the magnetic reflections and the studies presented below are first steps towards such spin-density measurements. Note that X-rays with energies around 100 keV are sensitive to the spin moments only, as shown in §2. This complements neutron diffraction, where the sum $2S + L$ of spin and orbital angular momentum is measured. By the combination of the results of measurements from the same crystal obtained with the two techniques, a separate determination of spin and orbital angular momentum should be possible.

The paper is organized as follows: In §2, we discuss the magnetic cross section for high-energy X-rays, to the extent that it differs from that for medium X-ray energies. In §3, the experimental set-up is presented. §4 contains a discussion of multiple scattering caused by *Umweganregung* and in §5 the results of the measurements are presented. A discussion of these results is given in §6. In §7, we give a short summary and conclusions.

2. The magnetic cross section for high-energy X-rays

Photon–electron scattering is in general a relativistic process and the scattering cross section should be calculated in a complete relativistic quantum-electro-dynamic framework to take into account all effects arising from the coupling of the quantized photon field and the Dirac field of the electrons.

Blume (1985) and Blume & Gibbs (1988) calculated the cross section for X-ray scattering including the magnetic terms from a non-relativistic Hamiltonian for electrons in a quantized electromagnetic field within second-order perturbation theory. The quasirelativistic formulation starts out from the Dirac Hamiltonian for an electron in an electromagnetic field. Then, the Fouldy–Wouthuysen transformation is applied to allow an interpretation in a non-relativistic form analogous to that obtained from the non-relativistic Hamiltonian (Platzman & Tzoar, 1970; de Bergevin & Brunel, 1981; Grotch, Kazes, Bhatt & Owen, 1983). The expansion of the transformed Hamiltonian depending on photon energy over electron rest mass $\hbar\omega/mc^2$ allows the description of the magnetic scattering process. Grotch, Kazes, Bhatt & Owen (1983) extended the Fouldy–Wouthuysen transformation to second order in $\hbar\omega/mc^2$. The dominating contribution to magnetic scattering is given by the first-order term. While the second-order term is sensitive to charge scattering only, the next magnetic contribution in the expansion is

expected from the third-order term. The strongest magnetic contribution stems from the first-order term and its interference term with charge scattering. The next-strongest magnetic contribution arises from the interference term between charge scattering and the third-order magnetic scattering. These interference terms are difficult to observe for antiferromagnets and in what follows we limit our discussion to the case of purely antiferromagnetic reflections, where the charge contribution vanishes. Possible applications of the interference terms for ferromagnetic materials are discussed by Brückel *et al.* (1993). In addition, for photons of energy $\hbar\omega \le 100$ keV, the third-order contribution to the cross section, being the next magnetic contribution, is reduced by a factor $1/25$ as compared to the first-order contribution (Lippert, Brückel, Köhler & Schneider, 1994). Therefore, these higher-order terms can be neglected in diffraction experiments with high-energy photons up to 100 keV. If the photon energy approaches the rest mass of the electron, $mc^2 = 511$ keV, $\hbar\omega/mc^2$ is no longer an appropriate expansion coefficient. In this case, a full relativistic treatment of the coherent magnetic scattering of X-rays is needed.

For the energy used for the experiments presented in this paper, the above expansion up to first order in $\hbar\omega/mc^2$ is valid to a very good approximation. Then, the scattering cross section for a transition from initial photon polarization state ε to final state ε' is given by

$$d\sigma/d\Omega|_{\varepsilon\to\varepsilon'} = r_0^2 |\langle M_C\rangle_{\varepsilon\varepsilon'} + i(\lambda_C/d)\langle M_M\rangle_{\varepsilon\varepsilon'}|^2. \quad (1)$$

λ_C denotes the Compton wavelength, $\lambda_C = h/mc$, d is the interplanar lattice spacing of the reflection under consideration and $r_0 = e^2/mc^2$ is the classical electron radius. The magnetic and the charge scattering amplitudes $\langle M_M\rangle$ and $\langle M_C\rangle$ are given in equations (4) and (5) of paper 1 in polarization-dependent matrices in a basis system, where σ and π represent the incident photon polarization perpendicular and parallel to the scattering plane, respectively (paper 1, Fig. 2). If only low-indexed reflections up to the MnF$_2$ 500 are considered for 80 keV photons, we can neglect terms with $\sin^2\theta \le 1/100$ in $\langle M_M\rangle$ and obtain the very simple expression

$$\langle M_M\rangle = \begin{array}{c|cc} & \sigma & \pi \\ \hline \sigma' & S_2 & 0 \\ \pi' & 0 & S_2 \end{array}. \quad (2)$$

Thus, the magnetic scattering is only sensitive to S_2, the Fourier transform of the spin component perpendicular to the scattering plane, parallel to $-\mathbf{k} \times \mathbf{k}'$. Obviously, there is no dependence on the orbital angular momentum for high energies and small scattering angles. To distinguish between scattering due to the spin and orbital angular momentums, two measure-

ments should be performed with photons and neutrons on the same crystal.

If higher-indexed reflections are considered, the foregoing simplification is not applicable. However, for MnF$_2$ we have only a spin moment (L = 0) and according to the experimental configuration $S_3 = 0$. The remaining term S_1 in the off-diagonal elements describes the spin component in the scattering plane perpendicular to the scattering vector, which is insignificant in our scattering geometry.

As a result, we measure purely magnetic scattering on the antiferromagnetic Bragg positions. Equation (1) considers a ε-polarized incident beam and a scattered beam of polarization ε'. For arbitrary polarization, the general expression for the magnetic differential cross section for high-energy photons at small scattering angles is obtained from the density-matrix formalism discussed by de Bergevin & Brunel (1981) and Blume & Gibbs (1988):

$$(\mathrm{d}\sigma/\mathrm{d}\Omega)_{\mathrm{magnetic}} = r_0^2(\lambda_C/d)^2|S_2^2|. \qquad (3)$$

For higher-indexed reflections and linear incident polarization, the magnetic scattering cross section can be expanded to second order in θ:

$$(\mathrm{d}\sigma/\mathrm{d}\Omega)_{\mathrm{magnetic}} = r_0^2(\lambda_C/d)^2[S_2^2(1 - \theta^2) - S_1^2\theta^2]. \qquad (4)$$

Finally, we want to point out some features valid for high-energy X-rays around 100 keV:

Polarization. Compared to medium-energy X-ray diffraction, the magnetic cross section (3) has no polarization dependence. Equation (2) shows that the cross section is completely independent of the polarization state of the incident beam. Moreover, for a linear σ- or π-polarized beam, there is no possibility of proving the magnetic character of a reflection by polarization analysis at small scattering angles. For larger scattering angles, σ-to-π scattering is suppressed by a factor $\sin\theta$ compared to σ-to-σ scattering. Note, however, that in the general case of arbitrary incident polarization a change of the polarization state can occur during magnetic Bragg diffraction.

Spin scattering. Equation (3) shows that there will be no signal from spin components lying in the scattering plane. If all spins of a macroscopic sample can be made to lie in the scattering plane by turning the sample around the scattering vector **Q**, the magnetically diffracted intensity tends to zero. This is possible for a monodomain crystal with collinear spin structure, for example. Note that this is a special case of the data presented in paper 1, Fig. 10 (Brückel *et al.*, 1996) for $\sin\theta \rightarrow 0$. For MnF$_2$ at an X-ray energy of 80 keV, the magnetic character of the 300 reflection has been proven by this method in a previous paper (Lippert, Brückel, Köhler & Schneider, 1994).

Volume enhancement. Owing to the large penetration depth of high-energy X-rays, an enhancement of the

cross section of several orders of magnitude can be obtained compared to the medium X-ray energies described in paper 1.

3. Experimental

The experiment was performed on the triple-crystal diffractometer at the white-beam station of the ESRF high-energy beamline ID15. The gap of the asymmetric wiggler was fully closed, thus gaining a critical energy of 43 keV with the storage ring operating at 6 GeV. The permanently installed cooled filters absorb the low-energy tail of the white beam in order to minimize the heat load on the monochromator. The beam size of 2 mm horizontal and 3 mm vertical is defined by cooled slits in front of the instrument. An energy of 80 keV was chosen where we knew from earlier experiments that there are regions in Ψ (rotation around the scattering vector) that are free of multiple scattering (Lippert, Brückel, Köhler & Schneider, 1994). The MnF$_2$ crystal is the same as in the experiments at HASYLAB (Brückel *et al.*, 1993, 1996; Lippert, Brückel, Köhler & Schneider, 1994). It has the form of a small platelet and the *a* axis is normal to the plate surface. The tetragonal *c* axis lies within the plate and is oriented almost along a diagonal of the rectangle (Fig. 1). To test the volume enhancement, the surface of the platelet was oriented parallel to the beam. Then, the sample
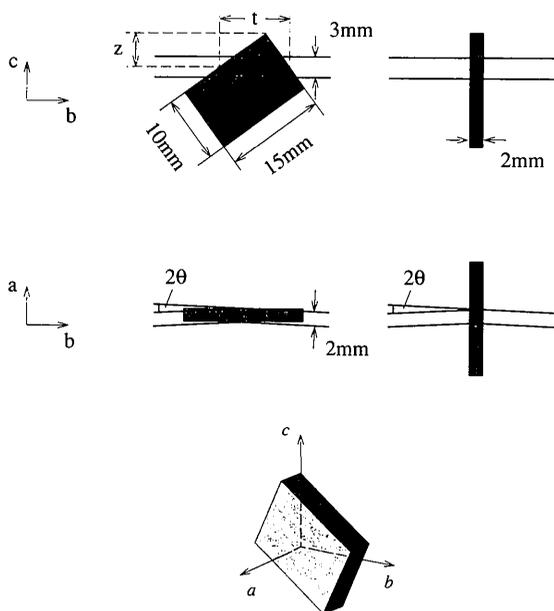
Fig. 1. Crystal geometries used in the experiment. On the left, the geometry with a variable beam path through the crystal is shown. On the right, the symmetrical Laue geometry with a constant beam path of 2 mm is shown. Below, a three-dimensional view of the crystal is plotted.

thickness seen by the beam, perpendicular to the c axis and parallel to the surface, is given by $t = z[\tan(90 - \varphi) + \tan\varphi]$, where $\varphi = 35.1°$ and $0 < z < 8.6$ mm is the position of the beam relative to the crystal starting from the upper edge and going to maximum thickness. For the measurement of the Q dependence and the temperature dependence of the intensity, the surface was oriented perpendicular to the beam. Note that in this Laue configuration geometrical factors are negligible owing to the small scattering angles.

Fig. 2 shows a sketch of the three-crystal diffractometer. The horizontal scattering geometry for monochromator, sample, analyzer and detector can be defined by moving the rotation stages independently on rails. The background is reduced by four collimators, which are mounted in front and between the stages, each with a horizontal opening of 5 mm. As monochromator and analyzer, we used imperfect Si 311 crystals in Laue geometry to get a nearly non-dispersive set-up in $(+, -, +)$ geometry for the magnetic 300 reflection of MnF_2. The respective lattice spacings are $d_{monochromator} = d_{analyzer} = 1.637 \text{Å}^{-1}$ and $d_{MnF_2,300} = 1.625 \text{Å}^{-1}$. The use of imperfect crystals with rocking-curve widths of $\sim 6''$ results in an intensity-enhancement factor of about 50 as compared to perfect Si crystals without significant degradation of resolution owing to the sample mosaicity of $12''$. In silicon, the 622 reflection is suppressed in intensity by a factor of 10^8 as compared to the 311 reflection, whereas the 933 and 12,4,4 reflections are allowed (Hart & Deutsch, 1990). There is no $\lambda/2$ contribution, whereas we had very strong $\lambda/3$ and $\lambda/4$ harmonics owing to the wiggler and beamline characteristics. While these higher harmonics can in general be suppressed owing to the energy resolution of the Ge detector by setting appropriate energy windows, they can lead to dead-time effects by saturating the detector. In the following, we will distinguish between a two- and a three-crystal mode of diffractometer operation depending whether the beam is diffracted only by monochromator and sample or also by the analyzer. In the three-crystal mode, we obtained a resolution of about 10^{-3}Å^{-1} longitudinal, $2 \times 10^{-4} \text{Å}^{-1}$ transversal and 10^{-2}Å^{-1} perpendicular to the scattering plane. The cryostat was an ILL-type Orange cryostat with an adapted ILL controller using two sets of calibrated Pt 100 and carbon resistors as temperature sensors for regulation and measurement, respectively. The cryostat was used as for neutron scattering experiments, *i.e.* without special windows. The 10 mm aluminium from the cryostat tails located in the beam resulted in an attenuation of the primary beam by 40%. For the measurements in the critical regime, we obtained a temperature stability of better than ± 0.001 K and the minimum temperature step near the phase transition was 0.01 K. In order to prevent the detector from saturation in the case of strong

reflections, the diffracted beam was attenuated by Fe and Pb absorbers. Since a monitor for the intensity of the incident beam was not available, we normalized the measured intensities with the electron ring current, which gave excellent reproducibility. This procedure is only possible because of the source stability and the fact that thermal effects due to the white beam hitting the monochromator are negligible: the low-energy tail of the spectrum is suppressed by the absorber down stream and most of the remaining hard X-rays are diffracted and not absorbed by the monochromator crystal.

4. Multiple scattering

Three-beam multiple charge scattering due to *Umweganregung* occurs if an additional reciprocal-lattice point lies on the Ewald sphere, as shown in Fig. 3. The effect has been discussed for diffraction of 411 keV γ-radiation from rather strong Bragg reflections (Schneider, 1975). However, *Umweganregung* is a very serious problem if the reflections investigated are weak. This is the case for the pure magnetic reflections of MnF_2, where the magnetic unit cell is the same as the structural one. Owing to the non-symmorphic space group of MnF_2, charge scattering at $2n + 1, 0, 0$ positions is forbidden by non-integral extinction rules only. Note that this is a very unfavorable situation for MnF_2 since integral extinction rules for non-primitive Bravais lattices rule out *Umweg* reflections. Therefore, in MnF_2, it is possible to get multiple charge scattering by a combination of two charge reflections transferring intensity to positions where otherwise only magnetic scattering is expected. The incoming photons are charge scattered twice to be finally diffracted in the same direction as the magnetically scattered photons. The condition for three-beam multiple scattering is that Q' and Q'' with $Q = Q' + Q''$ are allowed reflections. One way to suppress multiple scattering is to rotate the reciprocal lattice around the fixed scattering vector Q
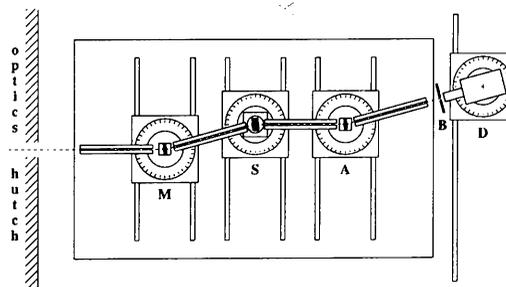
Fig. 2. Layout of the three-axis diffractometer at ID15 at ESRF in Grenoble. The rotation stages for monochromator M, sample S, analyzer A and detector D are mounted on rails to define the horizontal scattering geometry. The first three axes are built on an antivibrational table to avoid instabilities. The sample stage allows the cryostat to be mounted as used in this experiment. The slit B in front of the detector is used to define its aperture.

(Ψ rotation) until no other reflection touches the Ewald sphere. However, this is possible only for low energies. The probability of multiple-scattering events to occur increases with photon energy because the Ewald sphere becomes larger, increasing the probability that additional reciprocal-lattice points lie on the Ewald sphere. For high-energy photons, a temperature-independent modulated background due to multiple Bragg scattering is observed (Fig. 4) because there is always a large number of reflections with low intensities present on the Ewald sphere. A displacement of the maximum of this background relative to the nominal peak position occurs if the *Umweg* reflection is close to, but not exactly on, the Ewald sphere. Then, only the tails of the resolution function (Neumann, Rütt, Bouchard, Schneider & Nagasawa, 1994) cause multiple scattering. These resolution streaks extend outside the ideal ω_s position.

A typical Ψ scan is shown in Fig. 5. We have calculated three-beam multiple-scattering reflections using the program *MUSKAT* (Chernenkov, 1989) and were able to index the measured *Umweganregung* reflections. These reflections are very sharp in Ψ (with a width smaller than 0.01°) because low-indexed strong reflections pass the Ewald sphere in an almost

perpendicular direction during a Ψ scan (compare Fig. 3). Not all calculated *Umweganregung* reflections were observed in this Ψ range because the scan was too crude.

To investigate the behavior of multiple scattering as a function of photon energy, we take into consideration all reciprocal-lattice points within a shell around the Ewald sphere defined by the energy width of the photon beam. From the divergence of the beam incident on the
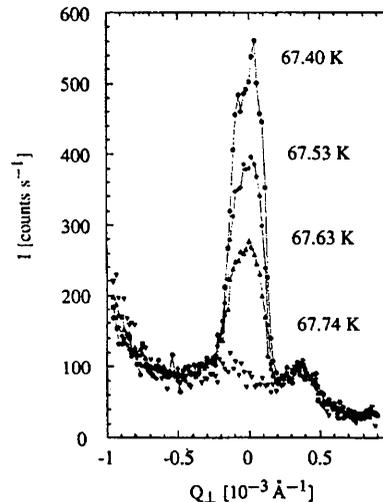
Fig. 4. Magnetic 300 reflections near T_N. The background around the Bragg reflection is temperature independent but modulated owing to multiple charge scattering. Because of the high Q space resolution and this background, no critical diffuse scattering could be observed.
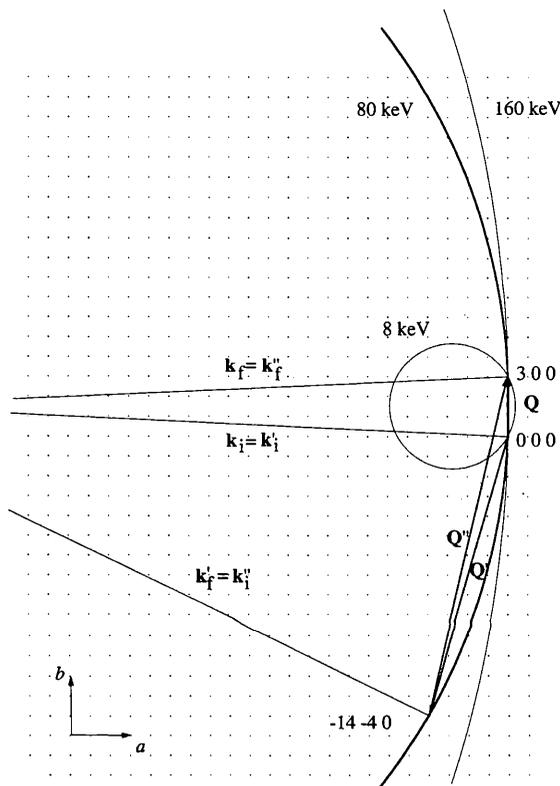
Fig. 3. Reciprocal lattice of MnF₂ in the *ab* plane. The intersections of the Ewald spheres are shown for different energies. **Q** denotes the scattering vector of the 300 reflections, **Q**′ that of an additional charge reflection $\overline{14},\overline{4},0$ on the Ewald sphere for 80 keV, **Q**″ is the effective scattering vector for the *Umweganregung* 17,4,0.
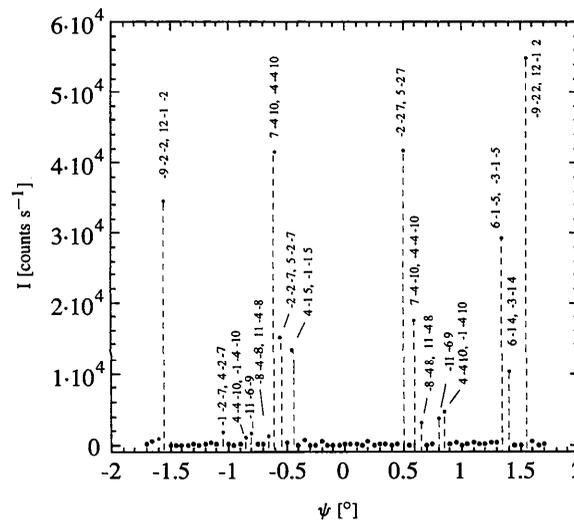
Fig. 5. Representative Ψ scan for the 300 magnetic reflection at 80 keV. The measured multiple-scattering events have been indexed by comparison with calculation. The respective multiple-scattering events are indexed by the reflections **Q**′ involved in the scattering process.

monochromator of 14″ and the width of the rocking curve of the 311 Si monochromator of 6″, the thickness of the Ewald sphere dk can be estimated according to d$k = k \cot \theta_M$ dθ, where θ_M is the Bragg angle of the monochromator and dθ the total beam divergence. All reflections between the two Ewald spheres with radius $k - dk/2$ and $k + dk/2$ are considered. The reflections are calculated from the atomic form factors of Mn^{2+} and F^- according to *International Tables for Crystallography* (1992), with the Debye–Waller factor for low temperatures taken from Jauch, Schultz & Schneider (1988).

First, we calculate the total scattered intensity from all Bragg reflections that can be excited. As indicated in Fig. 6, the full Q range $[0, 4\pi/\lambda]$ is divided into intervals $[Q_i, Q_i + \Delta Q]$ with $Q_i = i\Delta Q$, where Q is defined as $Q = 2\pi/d$. The average intensity P_i arising from *Umweganregung* of all reflections in this interval can be approximated in the following way:

$$I_Q^{um} \simeq I_{Q'} \times I_{Q''} \simeq \bar{I}_i^2 \quad \text{for} \quad Q \ll Q',$$
$$Q'' \in [Q_i, Q_i + \Delta Q], \quad (5)$$

$$P_i = \sum_{\substack{Q \in [Q_i, Q_i + \mathrm{d}Q] \\ Q \in V_{\mathrm{d}k}}} I_Q^{um} \simeq n_i \bar{I}_i^2. \quad (6)$$

Here, $I_{Q'}$ and $I_{Q''}$ are the intensities of the two charge reflections involved in the multiple-scattering process, explicitly calculated for MnF_2. $\bar{I}_i$ is the average Bragg
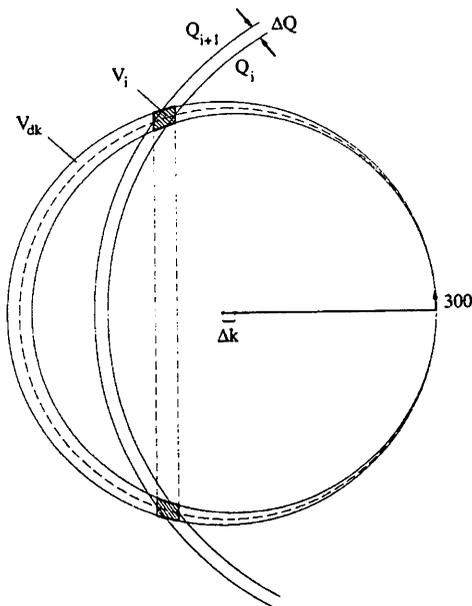
Fig. 6. Two-dimensional cut of the broadened Ewald sphere. $V_{\mathrm{d}k}$ denotes the volume between the two limiting spheres defined by the energy spread of the incident beam. Q_i and Q_{i+1} are the radii of two spheres around the origin. The hatched areas are cuts through the volume defined by the interval ΔQ and the Ewald sphere. In this figure, the thickness of the Ewald sphere is very exaggerated.

scattered intensity in the interval i, I_Q^{um} is the average scattered intensity due to *Umweganregung*, $V_{\mathrm{d}k}$ is the volume between the two Ewald spheres and n_i is the number of reflections in the volume V_i defined by the Q range $[Q_i, Q_i + \Delta Q]$ and the 'thickness' of the Ewald sphere (see Fig. 6). The approximation of considering *Umweganregung* via only high-indexed reflections Q' and Q'' is reasonable because only low-indexed magnetic reflections are measured. Then, we always have multiple scattering from two reflections in the same volume V_i. In Fig. 7, P_i is shown as a function of Q for a photon energy of 80 keV. The intensity scattered from the interval i is maximum for $Q = 5 \, \text{Å}^{-1}$. The total scattered intensity P_{tot}, shown in Fig. 8 as a function of energy, is given by

$$P_{\text{tot}} = \sum_i P_i. \quad (7)$$

Here, the sum runs over all shells i into which the volume $V_{\mathrm{d}k}$ of the Ewald sphere is divided. Above 30 keV, P_{tot} increases very slowly. While the number of strong multiple-scattering reflections remains constant, only very weak high-indexed reflections add to *Umweganregung* events.

In the following, we want to estimate first the number of strong reflections for small Q' to decide whether they can be suppressed by turning the crystal around the scattering vector. Second, we want to estimate the effect of reflections with small intensities for large Q'.

A large number of reciprocal-lattice points are located in the volume between the two Ewald spheres defined by $k - dk/2$ and $k + dk/2$. In our experiment, the magnetic reflections are by a factor of approximately 10^{-6} weaker than the strongest charge reflections and the peak-to-background ratio is of the order of 10^2. Therefore, we have to take into consideration all multiple charge scattering intensities greater than 10^{-8} of the strongest charge reflection.
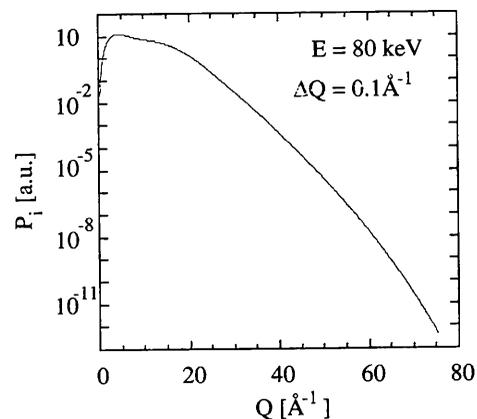
Fig. 7. Average intensity P_i due to multiple charge scattering in a Q interval $\Delta Q = 0.1 \, \text{Å}^{-1}$. P_i is plotted *versus* Q for 80 keV on a logarithmic scale.

In Fig. 9, we plot the average number of multiple-scattering events N_{tot}^K for any given Ψ position in the intensity interval $10^{-(K+1)} \le R_M/R_0 < 10^{-K}$. Here, R_M is the intensity of the multiple-scattering reflection and R_0 is the intensity of the strongest charge reflection. If N_{tot}^K is much larger than 1, multiple scattering cannot be suppressed by a Ψ rotation. As we remove one reflection from the Ewald sphere, others will enter this sphere. All events with $N_{tot}^K \simeq 1$ and smaller can be suppressed by a Ψ rotation. From Fig. 9, we see that *Umweganregung* events with intensities down to the 10^{-6} level can be suppressed by a Ψ rotation. Below the 10^{-8} level, we can expect a more-or-less constant background of multiple charge scattering at the magnetic Bragg positions. Note that N_{tot}^K undergoes only minor changes if we increase the photon energy
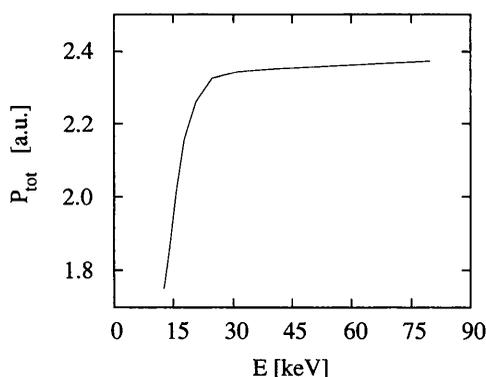
Fig. 8. Total scattered intensity P_{tot} due to *Umweganregung versus* photon energy. For a definition of P_{tot}, see text.
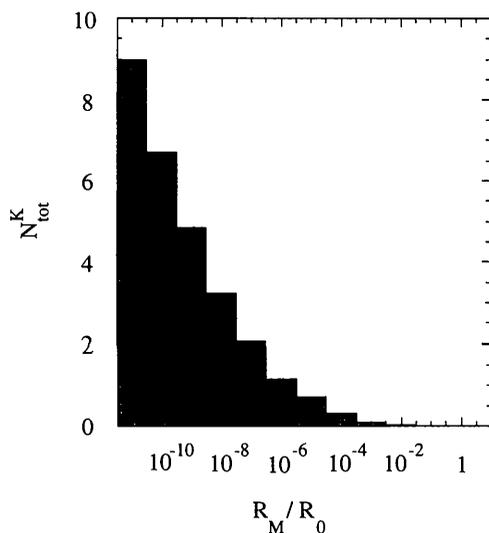
Fig. 9. Average number N_{tot}^K of multiple-scattering events for any given Ψ position in the intensity interval $10^{-(K+1)} \le R_M/R_0 < 10^{-K}$ *versus* the reflectivity of the multiple-scattering reflection normalized to the reflectivity of the strongest charge reflection R_M/R_0.

above 80 keV. Therefore, we expect to be able to suppress multiple charge scattering also at much higher photon energies. This is also evident from Fig. 8. Finally, we can calculate the average number of multiple-scattering events down to the 10^{-8} intensity level in a given Q interval from $Q = 0$ up to $Q = Q_{max}$. We find, for 80 keV, that above $Q = 18$ Å^{-1} there is always more than one reciprocal-lattice point on the Ewald sphere. Therefore, these weak high-indexed reflections contribute to the background. For all $Q \le Q_{max} = 18$ Å^{-1}, the multiple scattering can always be suppressed.

5. Magnetic diffraction from MnF$_2$

Figs. 10(a) and (b) show sample (ω_s) and analyzer (ω_a) scans of the 300 reflection in the three-crystal mode at 5 K. This corresponds to a transverse and a longitudinal scan, respectively. The peak widths of 12 and 5$''$ correspond to a Q-space resolution of 2×10^{-4} and 1×10^{-3} Å^{-1}, respectively. The peak intensity is about 12 000 photons s^{-1}. The same reflection measured in the two-crystal set-up (Fig. 10c) shows a width of 13$''$ and a peak intensity of $\sim$19 000 photons s^{-1}. The peak-to-background ratios are 230:1 and 10:1, respectively.

The enhancement of the intensity of the magnetic Bragg reflections with increasing sample volume is shown in Fig. 11 in the form of the linear dependency of the 300 integrated intensity on the average beam-path length through the crystal. This measurement in asymmetric Laue geometry was corrected for absorption. The variation of the average beam path from 0 to 18.3 mm was made possible by moving the crystal through the beam. The scattering geometry was discussed in §3. The transmission is calculated as $\int \exp(-\mu t) \, dV/V$ by integrating over all possible beam paths through the crystal, whose maximum linear dimension is more than twice the absorption length $l_{abs} = 1/\mu$. μ is the mass absorption coefficient which takes into consideration the photo effect and Compton scattering, the cross section for Rayleigh scattering being of minor importance for elements with low Z. For MnF$_2$, it is $\mu_{80keV} = 1.484$ cm^{-1}. μ has been calculated using the values for Mn and F from the program *ABSORPTION* (Brennan & Cowan, 1992).

The Q dependence of the reflectivity of the structural and magnetic reflections is shown in Fig. 12. These measurements are done in symmetric Laue geometry according to Fig. 1. For a measurement of the charge reflections, the diffracted beam has to be attenuated to avoid saturation of the detector. We employed an absorber of 2 mm Pb and 18 mm Fe to measure the charge reflections, which leads to a transmission of 1.1×10^{-6} for 80 keV, 3.9×10^{-2} for 240 keV (third harmonic) and 0.103 for 320 keV (fourth harmonic) after Brennan & Cowan (1992). Since for a completely closed wiggler gap the energy spectrum extends to very

high energies, the saturation of the detector due to higher harmonics can be a serious problem. In our case, we could not measure the 200 reflection reliably, which would become possible only by opening the wiggler gap. Therefore, only three reflections $h00$ are left, namely 400, 600 and 800. Their reflectivity can be calculated using an approximation that considers only small secondary extinction and no primary extinction in the Laue scattering geometry (Zachariasen, 1967):

$$R_C^Q = Q(t/\cos\theta)\exp[-(\mu + gQ)t/\cos\theta], \quad (8)$$

where
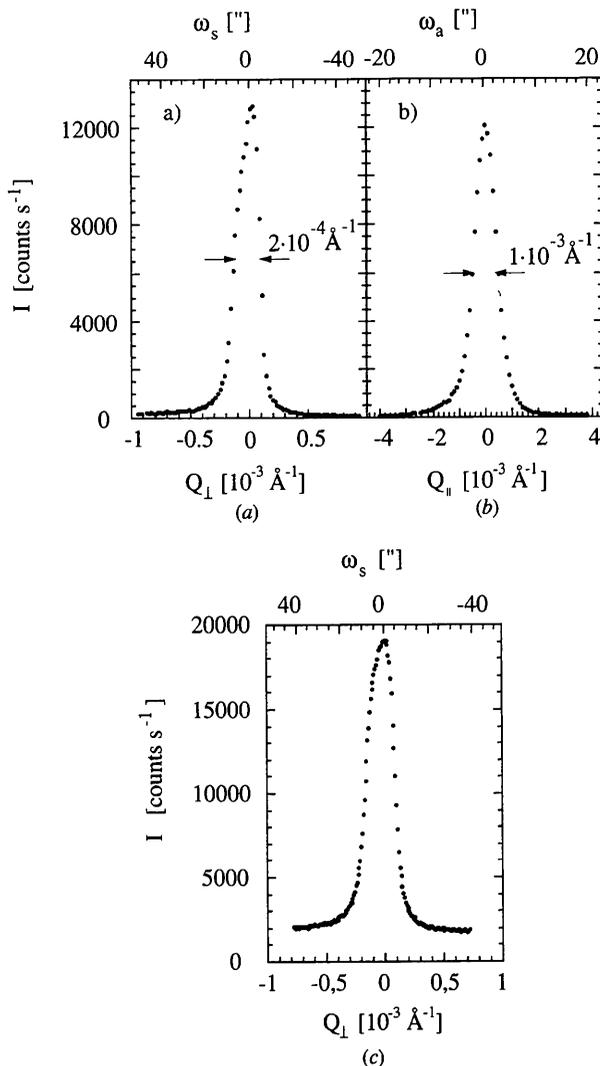
Fig. 10. Representative scans of the magnetic 300 reflection at $T = 5$ K. (a) and (c) show transversal scans in the three- and two-crystal modes, respectively. (b) shows a longitudinal scan in the three-crystal mode. The current in the ESRF storage ring was 104 and 115 mA for the scans in three- and two-crystal modes, respectively.

$$Q = r_0^2(1/V_{uc}^2)(\lambda^3/\sin 2\theta)|F_Q|^2. \quad (9)$$

μ is the linear mass absorption coefficient of MnF_2, λ the photon wavelength, t the thickness of the crystal, F_Q the structure factor and V_{uc} the volume of the unit cell. For small Bragg angles at 80 keV, the polarization factor is 1. The secondary-extinction factor has been calculated from the measured width of the sample rocking curve of the magnetic 300 reflection $\eta = 12''$ by $g = 1/2(\pi\eta)^{1/2}$ (Zachariasen, 1967) and gives a parameter-free theoretical curve. The primary extinction can be neglected because the extinction length for the 400 reflection of MnF_2 is $t_{ext} = 60$ μm. This is much larger than the expected size of perfect domains in our sample, which shows a mosaic spread of $12''$, 50 times larger than the width of the perfect crystal.

Magnetic reflections have been measured in the three-crystal mode from the 100 to the 700 reflection. For all magnetic reflections, we performed two-dimensional scans in reciprocal space in the three-crystal mode, i.e. sample scans on different analyzer positions, as shown for the 300 reflection in Fig. 13. In this way, we are able to determine the integrated intensities in the three-crystal mode. Additional scans in the two-crystal mode were performed, but are sometimes affected by small contributions of multiple charge scattering or dead-time effects from higher harmonics. According to (3), the reflectivity of the magnetic reflections can be described by

$$R_M^Q = r_0^2(\lambda_C/d)^2(\lambda^3/\sin 2\theta)(1/V_{uc}^2)f_{mag}^2|S_2|^2$$
$$\times (t/\cos\theta)\exp(-\mu t/\cos\theta), \quad (10)$$
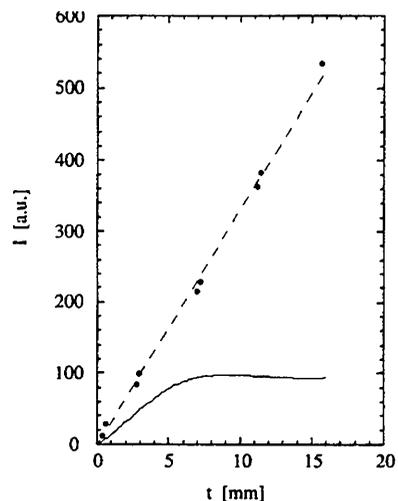
Fig. 11. The integrated intensity of the magnetic 300 reflection as a function of the beam path length through the crystal. The points show the measured intensity corrected for absorption. The dashed line represents the calculated intensity without absorption. The solid line shows the calculated intensity with absorption.

where f_{mag} is the magnetic form factor and S_2 the spin component perpendicular to the scattering plane. In contrast to (8), extinction is negligible for magnetic reflections. The reflectivity R_M^Q is proportional to $Q^2 f_{mag}^2$. This multiplication of the magnetic form factor by the magnitude of the scattering vector causes a peak in intensity between the reflections 100 and 300 and a less-rapid decrease of intensity with increasing Q, making high-indexed reflections accessible.

The measured intensity ratio between the magnetic 300 and the 400 charge reflection is 5.2×10^{-6}. The calculated ratio is 2×10^{-6}, taking in consideration the extinction of the charge reflections.

Finally, we have investigated the temperature dependence of magnetic scattering. The inset in Fig. 14 shows the temperature dependence of the intensity of the 300 reflection measured from 5 K up to 80 K. In order to minimize multiple charge scattering, we performed Ψ scans above the Néel temperature T_N and chose a region

in Ψ where the background of multiple scattering was low at the ω_s position of the 300 reflection. Fig. 4 shows the modulated background at the 300 position. This background is temperature independent, whereas the magnetic reflection disappears with increasing temperature.

From (3), it follows that the sublattice magnetization $M(T) \simeq S_2(T)$ is proportional to the square root of the magnetic Bragg intensity. In the critical temperature region just below T_N, the sublattice magnetization is expected to follow the power law

$$m = D\tau^\beta \qquad (11)$$

with the reduced coordinates

$$\tau = (T_N - T)/T_N, \qquad m = M(T)/M(0). \qquad (12)$$

Here, β denotes the critical exponent, T_N the Néel temperature and $M(0)$ the saturation magnetization. The scale factor D, the critical exponent and the critical temperature are determined from experiment.

The magnetic reflections measured with X-rays are free of extinction, in contrast to neutron measurements. In addition, the separation of diffuse scattering from true Bragg scattering is easier because of the high Q-space resolution. This allows a very accurate determination of β. To determine β, we subtracted the background, which is temperature independent, from the scans (compare with Fig. 4). In describing the integrated intensities by the squared power law (11), we obtained the best fit for data points in the temperature range from $T = 66.0$ K to $T = T_N$. The goodness of fit was 1.1. Fig. 14 shows the sublattice magnetization as a

Fig. 12. Q dependence of the reflectivity of charge (upper part) and magnetic (lower part) reflections. The dots represent measured values, the solid lines show the calculated behavior, rescaled to fit with the measurement.

Fig. 13. Contour plot of the magnetic 300 reflection at $T = 5$ K. The levels of the lines are 1000, 2000, 4000, 6000 and 8000 counts s^{-1}.
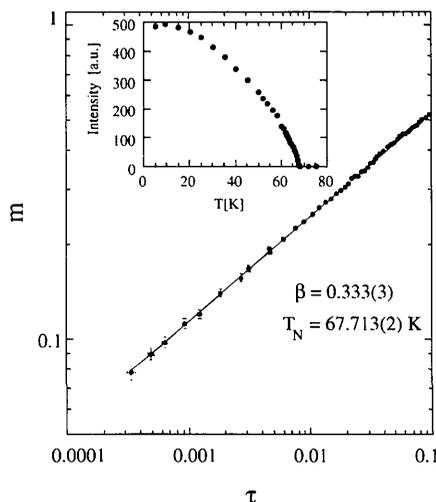
Fig. 14. The main graph shows the reduced magnetization $m = M(T)/M(0)$ as a function of the reduced temperture $\tau = 1 - T/T_N$ on a double logarithmic scale for the magnetic 300 reflection. The points are taken from the measurement, the solid line represents a fit using equation (11). The inset shows the temperature dependence of the intensity of the magnetic 300 reflection from 5 to 80 K with $T_N = 67.713$ K.

function of temperature in reduced coordinates and on a double logarithmic scale. For the parameters in (11), we find the following values: $\beta = 0.333\,(3)$, $T_N = 67.713\,(2)$ K and $D = 1.136$. The saturation magnetization, necessary for the calculation of D, was taken from a second independent measurement. For this reason, it is difficult to give an error estimation for D.

6. Discussion

As stated in the *Introduction*, our principal aim was to contribute to the development of non-resonant magnetic X-ray diffraction as a powerful microscopic probe of bulk magnetic properties, complementary to neutron diffraction. We believe that this aim has been reached by using very hard X-rays of 80 keV. The volume enhancement of diffracted intensities leads to high peak intensities of up to 19000 photons s^{-1}. This and the peak-to-background ratio of up to 230:1 compare very favorably to neutron diffraction and non-resonant X-ray diffraction at lower energies (see paper 1).

One major advantage over the traditional probe of neutron diffraction is the good transversal Q-space resolution of 10^{-4}, which is about two orders of magnitude better than in standard neutron diffraction. However, the high intrinsic resolution limits the applicability of the method to crystals with very narrow mosaic distribution and small $\Delta d/d$. For samples of poor quality, the peak broadens and the peak intensity decreases until the magnetic Bragg scattering merges into the background of Compton, charge disorder and thermal diffuse scattering. However, this limitation can be overcome if appropriate mosaic crystals can be found as monochromator and analyzer.

So far, we have applied the new method only to antiferromagnets where the magnetic Bragg scattering occurs at positions in reciprocal space where charge scattering vanishes. For ferromagnets, purely magnetic scattering cannot be observed on the high background of charge scattering. However, we pointed out earlier (Brückel *et al.*, 1993) that the charge–magnetic interference scattering should be particularly easy to measure at these high photon energies owing to the small scattering angles.

For antiferromagnets where the magnetic diffraction occurs at non-integral positions in reciprocal space, or at positions that are charge forbidden by integral extinction rules, charge scattering is no problem. This is the case for most antiferromagnets. MnF$_2$ is an exception, since charge scattering can occur owing to *Umweganregung* at positions where purely magnetic diffraction is expected. A large portion of the present study was devoted to the investigation of such multiple charge scattering events. We were able to demonstrate, *via* both experiment and calculation, that, despite the high probability for *Umweganregung* to occur at these high photon energies, multiple charge scattering can

largely be suppressed by turning the crystal around the scattering vector **Q**. Thus, the method is applicable to systems like MnF$_2$, too. While Fig. 4 shows that multiple charge scattering can lead to a modulated background, this modulation is negligible at saturation, where a peak count rate of 13000 photons s^{-1} has to be compared with the amplitude of the background modulation of about 100 photons s^{-1}. In the critical region, where the Bragg intensity is small, this background stays constant and can be corrected for by simply subtracting a high-temperature spectrum taken above T_N. By calculation, we demonstrate that the probability for multiple-scattering events first increases with photon energies but that this increase is negligible above 30 keV. Therefore, if 80 keV photons could be applied successfully in the present study, much higher photon energies could be used without additional complications. Only a higher background due to *Umweganregung* involving very high indexed charge reflections is expected. Our study of multiple scattering shows that this problem can be handled even at much higher energies than 80 keV.

The fundamental importance of the method becomes clear from an inspection of the magnetic scattering cross section (3). For energies around 100 keV, it depends only on the spin component S_2 perpendicular to the scattering plane. This allows the determination of spin density distributions *without* polarization analysis. While neutrons always measure the sum $2S + L$, medium-energy X-rays allow in principle the separate determination of S and L by means of polarization analysis. This rather complicated method involves a loss in count rate by typical factors of 50. Moreover, systematic errors, *e.g.* due to incomplete integrations over beam divergences, can easily occur. For these reasons, no convincing data for such an S, L separation exist to date. Here, our method of high-energy magnetic X-ray diffraction might provide a complementary powerful tool for the determination of $S(\mathbf{Q})$ without polarization analysis.

In this context, it is important to emphasize that the polarization of the incoming beam can be arbitrary, since it does not affect the scattering cross section (3). While this is certainly an advantage, the drawback is that the magnetic nature of a Bragg reflection cannot be identified by polarization analysis. For medium energies, we have demonstrated in paper 1 (Brückel *et al.*, 1996) how σ-to-π scattering can be used to identify magnetic Bragg scattering. In a first approximation, such a change in polarization does not occur for high-energy magnetic photon scattering, as can be seen from (2). Moreover, from an experimental point of view, polarization analysis at these high energies is not a trivial problem and new methods need to be developed. Keeping these arguments in mind, our Q-dependent reflectivity measurements shown in Fig. 12 can be considered as a first step towards such a

spin-density measurement. We could demonstrate that the magnetic form factor is weighted by the magnitude of the scattering vector. This, together with the intrinsic large Q range for very hard X-rays, allows the form-factor measurement to be extended to rather large Q values. Such form-factor measurements should be feasible with very high precision since systematic errors are expected to be very small: absorption is minor at these wavelengths and extinction can be completely neglected for the magnetic reflections owing to the small cross section and the short wavelength. However, Fig. 12 also demonstrates a general drawback of magnetic X-ray scattering as compared to neutron diffraction, namely the uncertainty of the normalization of magnetic Bragg intensities relative to charge scattering. Since the cross section differs by six orders of magnitude, uncertainties in the stoichiometry of the absorber material, its thickness and absorption coefficient become very important. Other ways of normalizing, e.g. by measuring the Compton scattered photons, will have to be considered.

Next, we want to discuss consequences of the volume enhancement demonstrated in Fig. 11. For transition-metal compounds with penetration depths of close to 10 mm, the volume enhancement amounts to roughly three orders of magnitude. For the heavier magnetic elements, similar factors can be achieved for smaller samples. For 150 keV, a typical penetration depth for lanthanides is 1 mm, for actinides 0.2 mm. Only for actinides are the enhancement factors observed in resonant exchange scattering larger compared to the volume enhancement expected for high-energy X-ray diffraction. However, the big advantage of the latter is the access to true bulk properties. Therefore, sophisticated surface-preparation techniques necessary for the observation of resonant exchange scattering can be avoided.

Finally, we want to discuss the temperature dependence of the sublattice magnetization in the critical region. Again, the traditional method for the investigation of critical phenomena is neutron diffraction. High-energy X-ray diffraction has distinct advantages as compared to this standard probe. For all diffraction techniques, crystals of high quality, i.e. narrow mosaic distribution, are required to clearly separate critical diffuse scattering from Bragg diffraction. However, neutron diffraction from close to perfect crystals suffers severely from extinction. Improper extinction corrections will result in systematic errors for the critical exponent β. This might be the reason for the absence of neutron diffraction measurements of β for MnF_2. This problem is absent in high-energy X-ray diffraction: the magnetic cross section and the wavelength are so small that the first Born approximation holds perfectly. Of course, this argument is also valid for medium X-ray energies around 10 keV. However, these probe only a near-surface region where the critical

behavior can easily be influenced by surface defects (Hill, Feng, Birgeneau & Thurston, 1993). Moreover, the intensities obtained for non-resonant X-ray diffraction are much smaller in this energy range (Goldmann et al., 1987). Finally, the need for X-ray-transparent windows makes it difficult to obtain the temperature stability required in the critical region. The combination of these factors explain the rather large standard deviation for the critical exponent obtained by Goldmann et al. (1987). Their value of $\beta = 0.31$ (2) is still in rough agreement with our value, $\beta = 0.333$ (3), but does not allow us to distinguish between different models.

Another highly precise study stems not from diffraction techniques but from a NMR investigation by Heller (1966). He obtained exactly the same critical exponent of $\beta = 0.333$ (3). The difference in Néel temperature of 67.713 (2) K (this work) and 67.336 K (Heller, 1966) lies within the usual uncertainties of the absolute temperature calibration. Heller argues that taking into account the effect of thermal expansion of the lattice changes the value of β to 0.335 (5). While the NMR technique proved very powerful in the case of MnF_2, it is not of the same general applicability as a diffraction technique. One drawback is that NMR measures the transferred hyperfine field at the ^{19}F nucleus and not the sublattice magnetization directly. Therefore, changes in the Mn—F distance can severely affect the critical behavior. Such an effect has indeed been observed in MnF_2 by Jauch, Schneider & Dachs (1983). Moreover, NMR cannot easily distinguish between long- and short-range order, an essential point for disordered materials, e.g. re-entrant spin glasses.

In our case of MnF_2, two independent experimental techniques obtain the same value of $\beta = 0.333$ (3). This value can be compared to theoretical values for β (Collins, 1989). The generally accepted values are $\beta = 0.326$ for the Ising model and $\beta = 0.367$ for the Heisenberg model. Clearly, our experimental findings are much closer to the value for the Ising model. This is to be expected owing to the pronounced uniaxial anisotropy in MnF_2 (spin directed along $\pm c$). However, for both independent measurements, the difference between the experimental and the theoretical values amounts to more than twice the e.s.d. This indicates that there is a systematic disagreement between experiment and theory. It might be that additional interactions have to be taken into account as has recently been shown in the case of EuTe (Köbler et al., 1993).

7. Summary and conclusions

In the present paper, we have demonstrated the capabilities of high-energy non-resonant magnetic X-ray diffraction on the model system MnF_2 at 80 keV. We have shown, both by experiment and by explicit calculation, that multiple charge scattering does

not hamper the observation of the magnetic signal, even at much higher energies. We demonstrated the volume enhancement of the magnetically scattered intensity by roughly three orders of magnitude. This leads to peak intensities for the magnetic 300 reflection of MnF_2 as high as $13\,000$ photons s^{-1} in three-crystal mode and $19\,000$ photons s^{-1} in two-crystal mode with peak-to-background ratios of 230:1 and 10:1, respectively. We argue that high-energy magnetic X-ray diffraction is sensitive to the spin moment only. Thus, our measurements of the Q dependence of the reflectivity of magnetic Bragg reflections can be regarded as a first step towards the determination of the pure spin-density distribution. Finally, we demonstrated the precision of magnetic structure-factor measurements on the investigation of the temperature dependence of the sublattice magnetization in the critical region. Here, the absence of extinction proved to be an essential point. Our results for the critical exponent $\beta = 0.333\,(3)$ agree very well with earlier NMR measurements but show a distinct difference to the theoretical value for Ising systems of $\beta = 0.326$.

The present measurements have demonstrated the capabilities of the method. Complete spin-density measurements should be possible now. Here, the advent of new sources for high-energy synchrotron radiation combined with high-quality sample crystals will make possible the measurement of systems with much lower magnetic moment. For example, at the new undulator beam line at the PETRA storage ring at DESY in Hamburg, we expect a flux gain by a factor of ten as compared to the present study.

References

Bergevin, F. de & Brunel, M. (1981). *Acta Cryst.* A37, 314-324.

Blume, M. (1985). *J. Appl. Phys.* 57, 3615-3618.

Blume, M. & Gibbs, D. (1988). *Phys. Rev. B*, 37, 1779-1789.

Brennan, S. & Cowan, P. L. (1992). *Rev. Sci. Instrum.* 63, 850-853.

Brückel, T., Lippert, M., Bouchard, R., Schmidt, T., Schneider, J. R. & Jauch, W. (1993). *Acta Cryst.* A49, 679-682.

Brückel, T., Lippert, M., Köhler, T., Schneider, J. R., Prandl, W., Rilling, V. & Schilling, M. (1996). *Acta Cryst.* A52, 427-437.

Chernenkov, Y. (1989). *MUSKAT. Program for the Calculation of Umweganregung.* ILL, Grenoble, France.

Collins, M. F. (1989). *Magnetic Critical Scattering*, p. 29. Oxford University Press.

Goldmann, A. I., Mohanty, K., Shirane, G., Horn, P. M., Greene, R. L., Peters, C. J., Thurston, T. R. & Birgenau, R. J. (1987). *Phys. Rev. B*, 36, 5609-5612.

Grotch, H., Kazes, E., Bhatt, G. & Owen, D. A. (1983). *Phys. Rev. A*, 27, 243-256.

Hart, M. & Deutsch, M. (1990). *Physica (Utrecht)*, A168, 66-74.

Heller, P. (1966). *Phys. Rev.* 146, 403-422.

Hill, J. P., Feng, Q., Birgeneau, R. J. & Thurston, T. R. (1993). *Z. Phys.* B92, 285-305.

International Tables for Crystallography (1992). Vol. C, edited by A. J. C. Wilson, pp. 487-503. Dordrecht: Kluwer.

Jauch, W., Schneider, J. R. & Dachs, H. (1983). *Solid State Commun.* 48, 907-909.

Jauch, W., Schultz, A. J. & Schneider, J. R. (1988). *J. Appl. Cryst.* 21, 975-979.

Köbler, U., Apfelstedt, I., Fischer, K., Zinn, W., Scheer, E., Wosnitza, J., Löhneysen, H. von & Brückel, T. (1993). *Z. Phys.* B92, 475-487.

Lippert, M., Brückel, T., Köhler, T. & Schneider, J. R. (1994). *Europhys. Lett.* 27, 537-541.

Neumann, H.-B., Rütt, U., Bouchard, R., Schneider, J. R. & Nagasawa, H. (1994). *J. Appl. Cryst.* 27, 1030-1038.

Platzman, P. M. & Tzoar, N. (1970). *Phys. Rev. B*, 2, 3556-3559.

Schneider, J. R. (1975). *J. Appl. Cryst.* 8, 530-534.

Schneider, J. R. (1995). *Synchrotron Radiat. News*, 8, No. 2, pp. 26-33.

Zachariasen, W. H. (1967). *Theory of X-ray Diffraction in Crystals*, pp. 156-168. New York: Dover.